YALE
PEABODY
MUSEUM

JOURNAL OF MARINE RESEARCH

The *Journal of Marine Research,* one of the oldest journals in American marine science, published important peer-reviewed original research on a broad array of topics in physical, biological, and chemical oceanography vital to the academic oceanographic community in the long and rich tradition of the Sears Foundation for Marine Research at Yale University.

An archive of all issues from 1937 to 2021 (Volume 1–79) are available through EliScholar, a digital platform for scholarly publishing provided by Yale University Library at https://elischolar.library.yale.edu/.

Requests for permission to clear rights for use of this content should be directed to the authors, their estates, or other representatives. The *Journal of Marine Research* has no contact information beyond the affiliations listed in the published articles. We ask that you provide attribution to the *Journal of Marine Research.*

Yale University provides access to these materials for educational and research purposes only. Copyright or other proprietary rights to content contained in this document may be held by individuals or entities other than, or in addition to, Yale University. You are solely responsible for determining the ownership of the copyright, and for obtaining permission for your intended use. Yale University makes no warranty that your distribution, reproduction, or other use of these materials will not infringe the rights of third parties.

The response of the coastal ocean to strong offshore winds: With application to circulations in the Gulfs of Tehuantepec and Papagayo

by Julian P. McCreary, Jr.,[1] Hyong S. Lee[1] and David B. Enfield[2]

ABSTRACT

Two ocean models are used to investigate the response of the coastal ocean to strong offshore winds: a linear 1½-layer model, and a nonlinear 1½-layer model that allows entrainment of cool water into the surface layer. The models are forced by wind stress fields similar in structure to the intense winter-time, mountain-pass jets (~20 dyne/cm²) that appear in the Gulfs of Tehuantepec and Papagayo for periods of 3–10 days. Solutions are arranged in a hierarchy of increasing dynamical complexity, in order to illustrate the important physical processes. They compare favorably with observations in several ways.

Some properties of solutions are the following. While the wind strengthens there is an ageostrophic current (not Ekman drift) that is directed *offshore*. This offshore drift forces coastal upwelling, thereby lowering the local sea level and sea surface temperature (SST). Although the drop in sea level at the coast can be large and rapid (of the order of 20 cm at the peak of a wind event), *none* of this signal propagates poleward as a coastally trapped wave. While the wind weakens the ageostrophic current is directed *onshore*, and consequently the coastal ocean readjusts toward its initial state. Throughout the wind event, cyclonic and anticyclonic gyres spin up offshore on either side of the jet axis due to Ekman pumping. Entrainment cools SST offshore, on and to the right (looking onshore) of the jet axis, and virtually eliminates the cyclonic gyre. The advection terms intensify the anticyclonic gyre and give it a more circular shape. After a wind event, the anticyclonic gyre propagates westward due to β. Its propagation speed is enhanced over that of a linear Rossby wave due to the nonlinear terms associated with the increased layer thickness at the center of the gyre and with the divergence of momentum flux.

1. Introduction

In the winter, high pressure systems, typically lasting from 3 to 10 days, develop in the Gulf of Mexico. These systems are almost everywhere separated from the Pacific region by the mountainous topography of southern Mexico and Central America. At three locations, however, there are passes through the mountains. During the high-pressure events, air flows swiftly through these passes down the resulting pressure

1. Nova University Oceanographic Center, 8000 N. Ocean Drive, Dania, Florida, 33004, U.S.A.
2. Atlantic Oceanographic and Meteorological Laboratories, 4301 Rickenbacker Causeway, Miami, Florida, 33149, U.S.A.
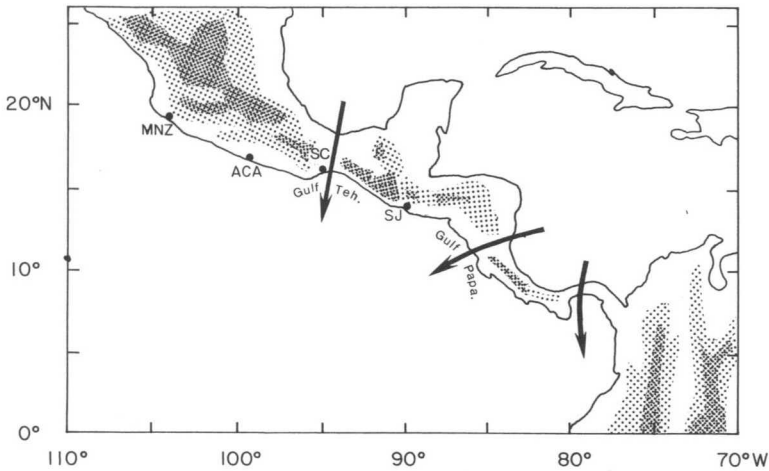
Figure 1. A map showing the locations of the three mountain-pass jets. Light and dark shaded regions indicate where the elevation of the topography is greater than 650 and 2000 m, respectively. The locations of Manzanillo (MNS), Acapulco (ACA), Salina Cruz (SC) and San Jose (SJ) are indicated. The jets occur during the winter when high-pressure systems develop over the Gulf of Mexico. Air flows rapidly through the mountain passes down the pressure gradients.

gradient, and forms narrow, intense jets in the Gulfs of Tehuantepec, Papagayo and Panama that blow almost directly offshore (Fig. 1). Roden (1961) has described the Tehuantepec jets (Tehuantepecers) in some detail. They have a width of about 200 km, extend southward about 500 km, and their strongest winds occur at the northern end of the Gulf. Based on a 12-year record, the mean maximum wind at Salina Cruz during fall and winter months was somewhat greater than 25 m/s, resulting in wind stress values of the order of 20 dyne/cm².

Roden also described aspects of the ocean's response to a Tehuantepecer. As the wind strengthens, water moves rapidly southward along the wind axis. Coastal currents as strong as 100 cm/s converge toward the jet axis, providing a source of water for the offshore current. Upwelling at the coast lowers sea surface temperature (SST) by about 10°C, and entrainment induced by the strong winds also cools SST farther offshore. Interestingly, on several cruises the lowest measured SST occurred offshore, suggesting that offshore entrainment is as significant as coastal upwelling. As the wind relaxes, the coastal ocean readjusts toward its initial state.

Figure 2 shows sea level and wind velocity at Salina Cruz during two Tehuantepecer seasons. There are a number of strong events where the wind attains speeds of the order of 10 m/s. (These wind events never achieve the strengths reported by Roden in this data set. The likely reason for this is that Salina Cruz is located at 16.10N, 95.12W, 25–30 km west of the mountain-gap axis, and so the wind recorder was not located in a position to measure the full strength of the jet. Generally, wind speeds from this station
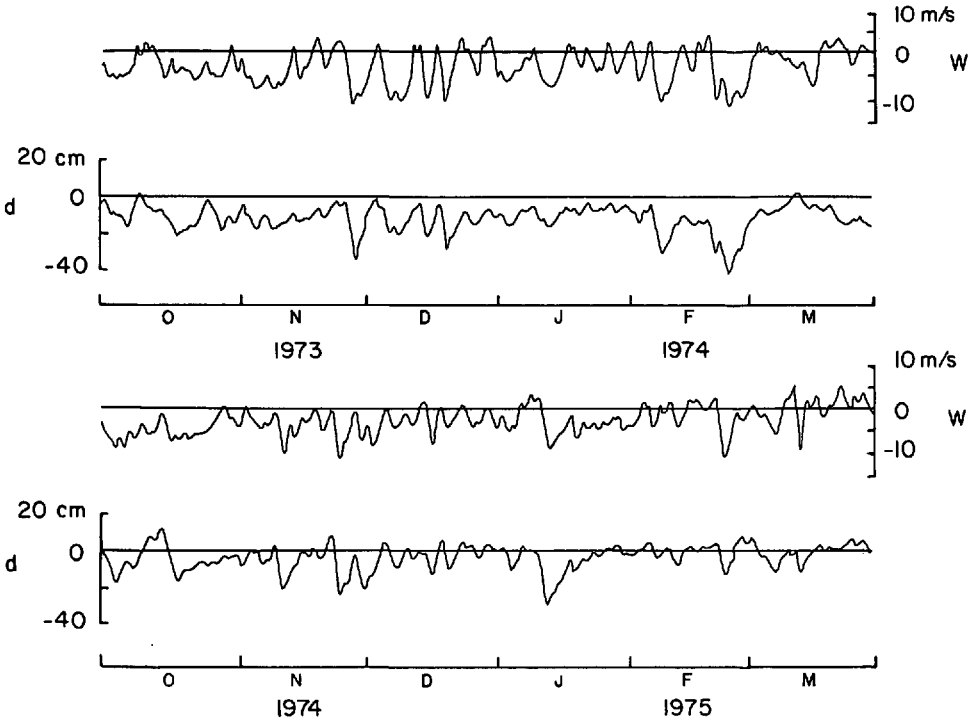
Figure 2. Wind velocity (w) and sea level (d) at Salina Cruz during the fall and winter of 1973/74 and 1974/75. Positive (negative) velocities are directed northward (southward). The close relationship between the two fields is apparent.

are about half as strong as those obtained offshore from ships.) There are also a number of events where sea level drops 20 cm or more in only a few days. The remarkable feature about the wind and sea-level variations is how closely related they are, indicating that the sea-level response follows the wind forcing with virtually no time lag.

Enfield and Allen (1983) looked for evidence of propagation of coastally trapped waves in sea level records along the Pacific coast of Mexico. Figure 3 shows four of the records (see Fig. 1 for their locations). Some events, particularly at lower frequencies, occur at all four stations, and they have phase lags that indicate poleward wave propagation. In contrast, the large, negative spikes in sea level at Salina Cruz do not occur at any other station. This property supports the idea that the spikes are locally forced by Tehuantepecers, and furthermore indicates that few or no coastal waves are generated by the forcing.

Stumpf (1975) and Stumpf and Legeckis (1977) presented satellite images of SST documenting the temporal and spatial development of the ocean's response to Tehuantepec and Papagayo wind events. Several of the images occur near the peak of
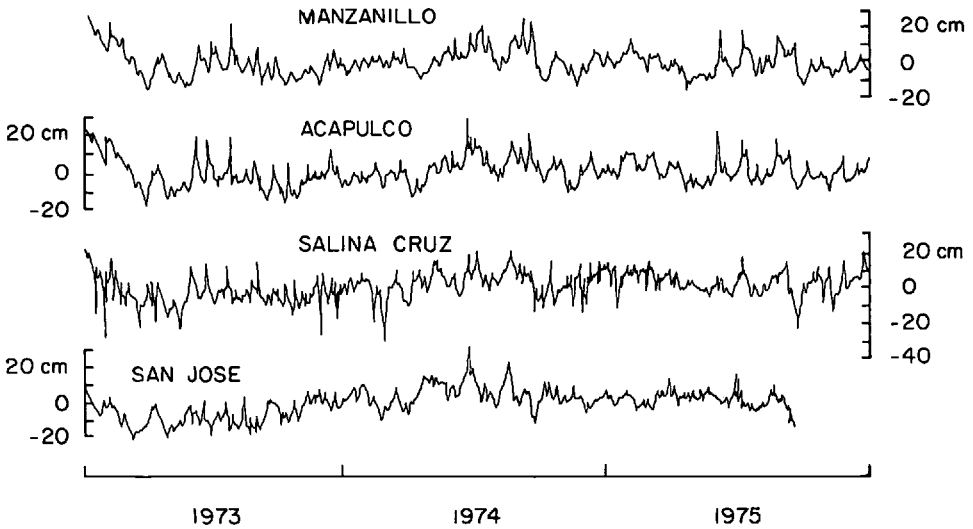
Figure 3. Sea level at San Jose, Salina Cruz, Acapulco and Manzanillo from 1973 through 1975. Figure 1 shows their locations. Negative spikes at Salina Cruz do not appear at San Jose, Acapulco or Manzanillo, suggesting that they are locally generated at Salina Cruz and that coastal waves are not part of the response. (After Enfield and Allen, 1983).

the wind (see, for example, Fig. 9 of Stumpf and Legeckis). In these images SST is coldest at the coast, but is also cooled significantly in a broad region offshore. Other images show the SST pattern a few days after an event (for example, Fig. 4 of Stumpf and Legeckis). In these images SST is coldest offshore, consistent with the cruise observations reported by Roden. The images also show that an anticyclonic gyre develops on the western flank of the jet axis. There is little evidence, however, that a second, cyclonic gyre forms on its eastern flank. Stumpf and Legeckis also noted that three anticyclonic Papagayo gyres, located at the coast and about 500 km and 1000 km offshore, occurred concurrently in their images, and suggested that they were due to three different wind events. Repeated views of the middle gyre were available, and it propagated westward with a phase speed of about 15 cm/s (13 km/day). Trajectories of drifting buoys indicate that Papagayo eddies continue to propagate westward at least to 115W, that is, a distance 2500 km offshore (Hansen, 1987; his Fig. 19).

Figure 4a, provided to us by Richard Legeckis, is an AVHRR thermal image of SST from off the coast of Central America and Mexico on February 25, 1986, that illustrates many of the features discussed above. The SST pattern reveals two Papagayo gyres: a small one spinning up near the coast (with its center near 88W, 12N), and a large one located offshore that is likely due to a previous Papagayo wind event. Tongues of warm and cold water near the edges of both gyres clearly show that they are anticyclonic. The region of coldest SST fans out offshore, suggesting the presence of a circulation that converges toward the jet axis near the coast and diverges offshore.
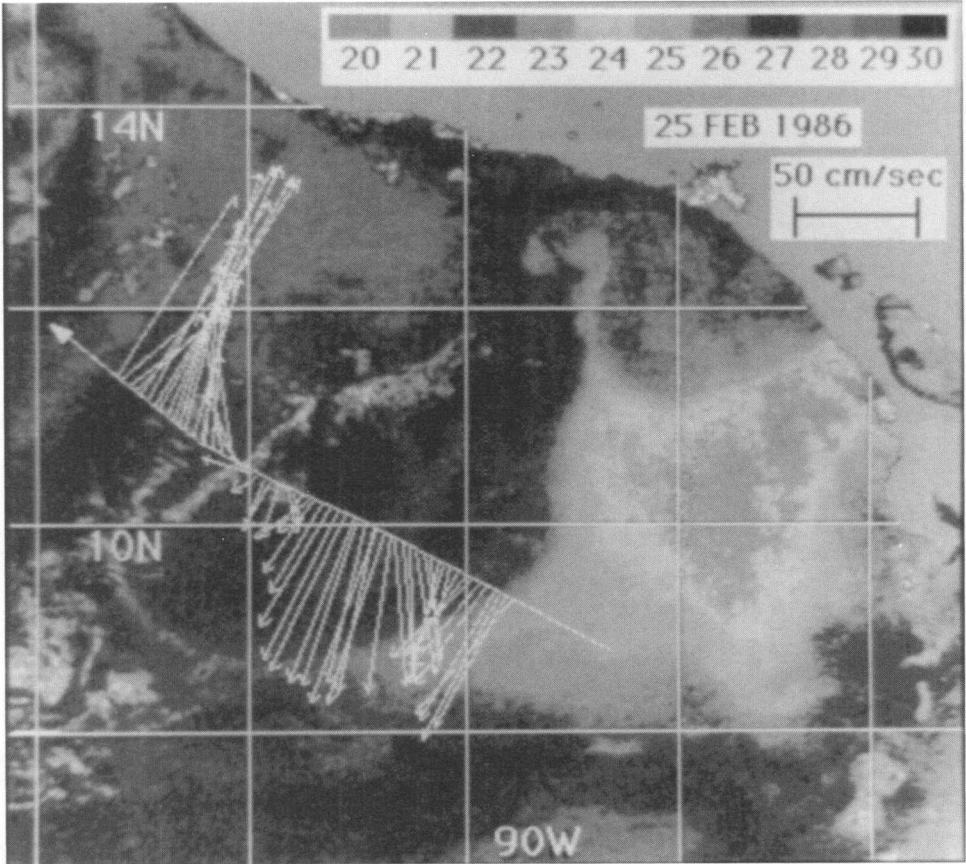
Figure 4a. An AVHRR thermal image showing SST in the vicinity of the Gulf of Papagayo on February 25, 1986, during a wind event. The spatial resolution of the image is 1 km. A region of cold SST spreads offshore along the axis of the jet. An anticyclonic gyre centered at 88W, 12N is developing on the western side of the cold tongue, with cold water being advected around its southern flank and warm water being advected southeastward along the coast. SST at the center of the gyre reaches a minimum of 23°C. A second larger gyre, presumably generated by an earlier event, is evident farther offshore, and minimum SST at its center is about 27°C. Superimposed arrows show near-surface, current measurements obtained on February 27, 1986, with the longest arrows indicating speeds somewhat greater than 80 cm/s. An upwelling event is also taking place in the extreme northwest corner of the figure in the Gulf of Tehuantepec. (The satellite image was provided by Richard Legeckis, and the current measurements by David Cutchin.)

The commercial tanker *Exxon Jamestown,* en route from Panama to San Diego, crossed the large eddy on February 26–27, only a day or two after the satellite image was taken. The ship was equipped with an acoustic Doppler current profiler (ADCP) which measured the eddy structure from 20 to 120 m. Data from this section, provided to us by David Cutchin, are shown in both Figures 4a and 4b. The 20 m currents
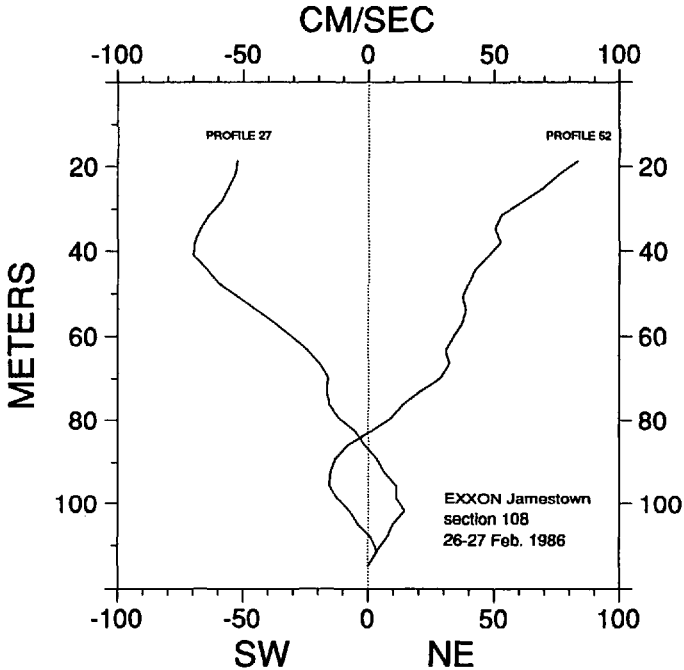
Figure 4b. ADCP velocity profiles near the current maxima on either side of the large eddy in Figure 4a. The current measurements were obtained on February 27, 1986, by means of an ADCP mounted on the volunteer observing ship *Exxon Jamestown.* The nominal random error of a single ADCP measurement is about 40 cm/s and 400 measurements go into each 15-minute average; therefore, the averaging reduces the uncertainty to 2-3 cm/s for each profile. Profile 27 is on the southeast side of the eddy, whereas profile 52 is on the northwest side. The flow field is confined to the upper 100 m. (The data were provided by David Cutchin.)

(relative to zero at 112 m) are shown superimposed on the image (Fig. 4a), and they corroborate the clockwise rotation of the offshore gyre at speeds of the order of 80 cm/s. Figure 4b shows two of the profiles, one near the maximum flow on each side of the eddy. They reveal a highly baroclinic structure confined to the upper 100 m.

In this paper, we investigate the ocean's response to forcing by strong wind fields that are directed offshore, like the mountain-pass jets. Two ocean models are used: a linear 1½-layer model, and a nonlinear 1½-layer model that includes entrainment of cool water into the surface layer. In order to illustrate clearly the important physical processes, solutions are arranged in a hierarchy of increasing dynamical complexity, varying from linear, analytic solutions to fully nonlinear, numerical ones. The numerical solutions are able to simulate all of the observed features discussed above. The analytic solutions are similar to some of the solutions discussed by Crepon and Richez (1982), but differ in that our wind fields have more general temporal and

spatial structures; similarities and differences between their solutions and ours are pointed out in the Appendix. The 2-layer numerical model used by Hua and Thomasset (1983) is dynamically similar to ours, including both entrainment and forcing by offshore winds, and it is instructive to compare the solutions to both models.

2. The model oceans

a. The linear model

The 1½-layer model has a single, active layer of density ρ_1 overlying a deep, inert layer of density ρ_2 where the pressure gradient is set to zero. Linearized equations of motion for the system are

$$u_t - fv + p_x = \tau^x/H + \nu_h\nabla^2 u,$$
$$v_t + fu + p_y = \tau^y/H + \nu_h\nabla^2 v, \tag{1a}$$
$$h_t + H(u_x + v_y) = 0,$$

and

$$p = g'(h - H). \tag{1b}$$

The velocities u and v are directed eastward and northward, respectively, the instantaneous thickness of the surface layer is h and its initial value is H, p is the pressure in the layer, f is the Coriolis parameter, ν_h is the coefficient of horizontal eddy viscosity, $g' = (\Delta\rho/\bar{\rho})g$ where $\Delta\rho = \rho_2 - \rho_1$, $\bar{\rho}$ is the average density, and g is the acceleration of gravity. The ocean can be forced either by a meridional wind field τ^y or by a zonal wind field τ^x. Finally, sea level d is related to p and h by

$$d = p/g = (\Delta\rho/\bar{\rho})(h - H). \tag{2}$$

Eqs. (1b) and (2) follow from the assumption that the pressure gradient vanishes in the deep ocean.

Analytic solutions to Eqs. (1) are found without horizontal mixing in either an unbounded basin or a semi-infinite basin with a northern boundary at $y = 0$. In the latter case, a single boundary condition of no-normal-flow is imposed at the northern boundary, and the solutions are required to remain finite in the far field. Numerical solutions are found in a rectangular basin with northern and eastern boundaries representing the southern coast of Mexico and the western coast of Nicaragua, respectively. Boundary conditions on the northern, eastern and southern boundaries are the no-slip conditions

$$u = v = 0, \tag{3a}$$

and on the western boundary are the open conditions

$$u_x = v_x = 0. \tag{3b}$$

The western and southern boundaries, of course, are artificial, but various test runs indicated that they did not significantly influence the model response.

Numerical solutions are evaluated on a staggered grid with variables defined in rectangular grid boxes of dimension Δx by Δy. The h points are located in the middle of grid boxes, and the u and v points are centered on their meridional and zonal edges, respectively. The equations of motion are forward differenced in time using the leap-frog scheme, and all fields are averaged between two time levels every 41 time steps in order to control time-splitting instability. Diffusive terms are evaluated at the backward time level, and all other terms at the central time level. For all the solutions shown in the figures, the grid dimensions are $\Delta x = \Delta y = 20$ km, and the time step is $\Delta t = 30$ min. In order to determine more accurately the values of variables very near the coast, some calculations are also carried out on a finer grid with $\Delta x = \Delta y = 5$ km and $\Delta t = 5$ min.

b. *The nonlinear model*

This model is very similar to the 2½-layer model described in McCreary and Kundu (1988), except that it involves only one active layer. For this reason, only a brief description of the equations of motion and boundary conditions is provided here, and readers interested in additional details should consult the previous paper. Except for test calculations, the equations of motion are

$$(hu)_t + (uhu)_x + (vhu)_y - fhv + hp_x = \tau^x + \nu_h\nabla^2(hu),$$
$$(hv)_t + (uhv)_x + (vhv)_y + fhu + hp_y = \tau^y + \nu_h\nabla^2(hv), \qquad (4a)$$
$$h_t + (hu)_x + (hv)_y = w_e,$$
$$T_t + uT_x + vT_y = Q/h - w_e(T - T_d)/h + \kappa_h\nabla^2 T,$$

and the pressure gradient is

$$\nabla p = \epsilon g\nabla[h(T - T_d)] - \tfrac{1}{2}\epsilon gh\nabla T. \qquad (4b)$$

Common variables are defined the same as in Eqs. (1). Additional quantities are T and T_d, the temperatures in the surface layer and deep ocean, respectively, and ϵ is the coefficient of thermal expansion (assumed constant). Three thermodynamic processes affect T: the heat flux Q through the ocean surface, horizontal diffusion of heat with coefficient κ_h, and entrainment described by the velocity w_e. According to (4a), the system entrains lower-layer water into the upper layer at the rate w_e, but detrainment (where $w_e < 0$) is not allowed. Sea level is given by

$$d = \epsilon[h(T - T_d) - H(T_0 - T_d)], \qquad (5)$$

where T_0 is the initial value of T. Eqs. (4b) and (5) follow directly from the two assumptions that the pressure gradient vanishes in the deep layer, and that currents in the surface layer remain depth independent.

The surface heat flux is given by

$$Q = \frac{H}{t_h}(T_0 - T), \tag{6}$$

a form similar to the one proposed by Haney (1971). According to (6), t_h is a measure of the e-folding time for the upper-layer temperature to relax back to T_0. Our solutions are not sensitive to the value of t_h, provided that it is sufficiently large (≥ 25 days).

Entrainment is a crucial process in the model. It acts to cool the upper layer, to provide stress at its bottom, and to prevent the interface between the two layers from surfacing. Entrainment is defined by the choice for entrainment velocity w_e, and following McCreary and Kundu (1988) we adopt the smooth function

$$w_e = \begin{cases} \dfrac{(H_e - h)^2}{t_e H_e}, & h < H_e \\ 0, & \text{otherwise.} \end{cases} \tag{7}$$

According to Eq. (7), entrainment exists only when h is less than a specified value H_e, and w_e increases parabolically toward a maximum value of H_e/t_e as h goes to zero. The entrainment time scale t_e must be chosen small enough to ensure that the interface does not surface in regions of intense upwelling, but otherwise solutions are not particularly sensitive to its value. Solutions, however, are affected by the choice of H_e (see the discussion at the end of Section 3d).

Boundary conditions on the northern, eastern and southern boundaries are

$$u = v = T_n = 0, \tag{8a}$$

where the subscript n indicates the partial derivative normal to the boundary, and on the western boundary are

$$u_x = v_x = T_x = 0. \tag{8b}$$

The conditions on T ensure that there is no heat flux through the boundaries.

The numerical scheme is essentially the same as that of the linear, $1\frac{1}{2}$-layer model, except that it involves a temperature equation for T. The T field is evaluated at the same points as h, that is, in the centers of grid boxes. The grid dimensions and time step are the same as those given above.

3. Results

In order to illustrate clearly the important physical processes, the solutions reported here are arranged in a hierarchy of increasing dynamical complexity. Inviscid, analytic solutions are found on the f-plane in several different situations: for a spatially uniform wind in both an unbounded and a semi-infinite ocean, and for a spatially bounded wind patch. Numerical solutions illustrate the effects of horizontal mixing, entrainment, beta and nonlinearities.
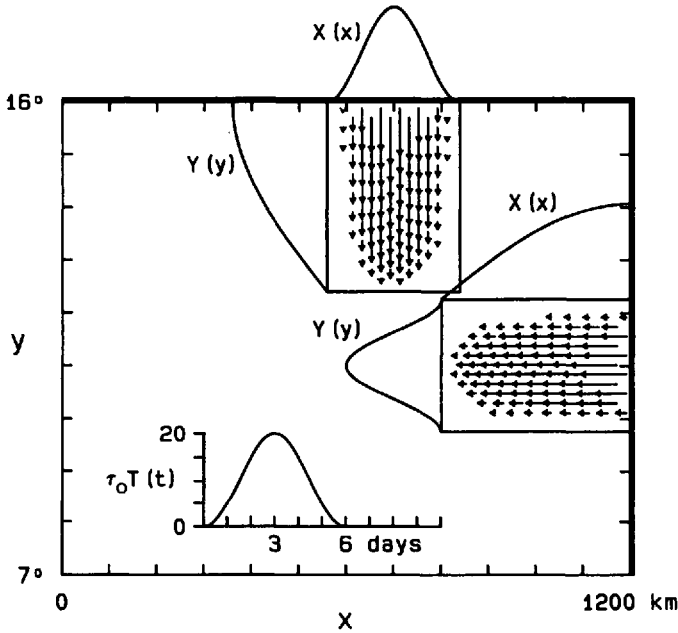
Figure 5. A schematic diagram illustrating the spatial and temporal structures of the wind fields forcing the Tehuantepec and Papagayo solutions. Both jets are directed offshore, are 280 km wide and 400 km long, and the absolute value of the maximum stress is 20 dyne/cm².

a. Choice of parameters

The model oceans are forced by wind fields similar to the Tehuantepec and Papagayo jets. They both have the separable form

$$\tau = \tau_o X(x) Y(y) T(t), \qquad (9)$$

where τ is always directed offshore. Figure 5 shows the locations of the wind fields, as well as their offshore and alongshore structures, $X(x)$ and $Y(y)$. For the Tehuantepec wind, the horizontal structure is

$$X(x) = \begin{cases} \dfrac{1}{2}\left[1 + \cos\dfrac{2\pi(x - x_m)}{x_w}\right], & |x - x_m| < x_w/2 \\ 0, & \text{otherwise,} \end{cases} \qquad (10)$$

where $x_m = 700$ km and $x_w = 280$ km, and the meridional structure is

$$Y(y) = \begin{cases} \cos\dfrac{\pi(y - y_m)}{2y_w}, & y > y_m - y_w \\ 0, & \text{otherwise,} \end{cases} \qquad (11)$$

where $y_m = 16N$ and $y_w = 400$ km. For the Papagayo wind, the structures are similarly defined, with x and y interchanged and with $x_m = 1200$ km and $y_m = 11N$. The figure also shows the time dependence of the wind, defined by

$$T(t) = \begin{cases} \dfrac{1}{2}\left[1 - \cos\dfrac{2\pi t}{t_w}\right], & t < t_w \\ 0, & \text{otherwise} \end{cases} \tag{12}$$

with $t_w = 6$ days. The amplitude of the wind is $|\tau_o| = 20$ dyne/cm^2 for all the solutions shown.

Ocean parameters are set as realistically as possible. The initial value for upper-layer thickness is $H = 50$ m, and initial temperatures are $T = T_0 = 29°C$ and $T_d = 12°C$. The thickness H is a typical value for the depth of the sharp pycnocline near Tehuantepec, and T_0 and T_d are typical temperatures above and below the pycnocline. The coefficient of thermal expansion has the constant value 3×10^{-4} °C^{-1}. With these choices, $\Delta\rho/\bar{\rho} = \epsilon(T_0 - T_d) = .0051$ and the characteristic speed of the system is $[(\Delta\rho/\bar{\rho})gH]^{1/2} = 158$ cm/s.

Unless specified otherwise, the horizontal mixing coefficients are $\nu_h = \kappa_h = 2 \times 10^7$ cm^2/s, and the thickness below which the upper layer starts to entrain is $H_e = H = 50$ m. The thermodynamic time constants are $t_h = 50$ days and $t_e = \frac{1}{8}$ day. The small value for t_e is necessary in order to prevent the interface between layers from surfacing at the coast.

Finally, the Coriolis parameter f is either constant or it is given by $f = 2\Omega \sin(y/R)$, where $\Omega = 2\pi/$day and R is the radius of the earth. When f is constant, it has the value $f = 2\Omega \sin(16°) = 4.0 \times 10^{-5}$s^{-1} for the Tehuantepec case and $f = 2\Omega \sin(11°) = 2.77 \times 10^{-5}$s^{-1} for the Papagayo case.

b. Analytic solutions

i. Uniform meridional wind, unbounded ocean. For this solution the forcing has the form $\tau^y = \tau_o T(t)$, f is constant, and the ocean's response is spatially uniform. Neglecting all x and y derivatives in the inviscid version of (1), and taking Laplace transforms (designated by a carat), yields the expressions

$$\hat{u} = \frac{f\tau_o}{H}\frac{\hat{T}(s)}{s^2 + f^2}, \qquad \hat{v} = \frac{s}{f}\hat{u}, \qquad \hat{p} = 0. \tag{13}$$

The inverse Laplace transforms can be easily found using the convolution theorem, but it is more useful to invert (13) when $T(t)$ varies slowly with respect to the inertial period f^{-1}. In that case, an approximate solution can be found by neglecting s^2 in the denominators of $\hat{u}$ and $\hat{v}$ (see the discussion in the Appendix). This approximation filters inertial oscillations out of the response, and is valid because they are not strongly

excited by a slowly varying wind. The resulting solution is

$$u = \frac{\tau_o}{fH} \mathcal{T}(t), \quad v = \frac{\tau_o}{f^2 H} \mathcal{T}_t, \quad p = 0, \tag{14}$$

which describes a zonal Ekman drift, and an additional, ageostrophic, meridional current proportional to the time derivative of the wind. It is the latter current, rather than Ekman drift, that drives coastal upwelling in all subsequent solutions.

For the time dependence defined in (12), the meridional current is given by $v = (\tau_o \pi / f^2 H t_w) \sin (2\pi t / t_w)$ for $t < t_w$ and is zero thereafter. When the wind is southward $(\tau_o < 0)$, v is also southward during the first 3 days while the wind strengthens, and is northward from day 3 to day 6 as it relaxes. For the parameter values discussed above with $f = 4.0 \times 10^{-5} \mathrm{s}^{-1}$, the maximum speed of the drift (at 1.5 and 4.5 days) is 15.2 cm/s. In contrast, the maximum Ekman drift (at 3 days) is 100 cm/s, much stronger than the meridional current.

ii. Uniform meridional wind, semi-infinite basin. When there is a boundary at $y = 0$, a free solution must be added to (13) that brings v to zero at the coast. It follows that

$$\hat{u} = \frac{f \tau_o}{H} \frac{\hat{\mathcal{T}}(s)}{s^2 + f^2} (1 - e^{\kappa y}), \quad \hat{v} = \frac{s}{f} \hat{u}, \quad \hat{p} = \frac{\tau_o}{H\kappa} \hat{\mathcal{T}}(s) e^{\kappa y}, \tag{15}$$

where $\kappa = (s^2 + f^2)^{1/2}/c$ and $c = \sqrt{g'H}$ (see the Appendix). Again, with the approximation that the wind is slowly varying, the inversion is easy, and the solution is

$$u = \frac{\tau_o}{fH} (1 - e^{\alpha y}) \mathcal{T}(t), \quad v = \frac{\tau_o}{f^2 H} (1 - e^{\alpha y}) \mathcal{T}_t, \quad p = \frac{c\tau_o}{fH} e^{\alpha y} \mathcal{T}(t), \tag{16}$$

where $\alpha = f/c$ is the reciprocal of the Rossby radius of deformation.

It is interesting that the Ekman drift u [for convenience, defined here and in subsequent discussions to include the coastally trapped term proportional to $\exp (\alpha y)$] vanishes at the coast, even though the boundary condition only requires that $v = 0$ there; thus, no coastal jet is generated by the wind. This property follows directly from the first of Eqs. (1a), which in this case simplifies to $u_t = 0$ at the coast. Another feature of the solution is that there is a coastal pressure field that is directly proportional to the wind stress. This pressure field is caused by the divergence (convergence) of v at the coast; the interface must rise (fall) in order to provide a source (sink) for the displaced water.

According to (16) and (2), sea level at the coast is $d = (c\tau_o/fgH)\mathcal{T}(t)$. For the parameter choices discussed above and the time dependence (12), the maximum drop in sea level (at 3 days) is 16.1 cm.

iii. Wind patch, semi-infinite basin. For this solution the forcing has the spatially limited form (9) and f is constant. With the assumptions that the wind is slowly varying in time with respect to f^{-1} and large-scale in x and y with respect to α^{-1}, the solution is

$$u = \underbrace{\frac{\tau_o}{fH} X[Y - Y(0)e^{\alpha y}]\mathcal{T}}_{u_1} + \underbrace{\frac{c^2\tau_o}{f^2H} X_x[Y_y - \alpha Y(0)e^{\alpha y}] \int_0^t \mathcal{T}(r)\, dr}_{u_2},$$

$$v = \underbrace{\frac{\tau_o}{f^2H} X[Y - Y(0)e^{\alpha y}]\mathcal{T}_t}_{v_1} - \underbrace{\frac{c^2\tau_o}{f^2H} X_{xx}[Y - Y(0)e^{\alpha y}] \int_0^t \mathcal{T}(r)\, dr}_{v_2}, \qquad (17)$$

$$p = \underbrace{\frac{c\tau_o}{fH} XY(0)e^{\alpha y}\mathcal{T}}_{p_1} - \underbrace{\frac{c^2\tau_o}{f^2H} XY_y\mathcal{T}}_{p_{1'}} - \underbrace{\frac{c^2\tau_o}{fH} X_x[Y - Y(0)e^{\alpha y}] \int_0^t \mathcal{T}(r)\, dr}_{p_2}.$$

The derivation of this approximate solution is somewhat lengthy, and is provided in the Appendix. In fact, with $X(x)$ given by (10) the wind is too narrow to be large-scale in x, and consequently (17) has features that are not accurate; for example, it overestimates the maximum currents and sea-level response. Nevertheless, the solution is still useful because its basic structure and time development is correct, and because it reveals all the important physical processes in a simple way.

The terms labeled with the subscript 1 in (17) are the direct counterparts of those in solution (16). The pressure field $p_{1'}$, like p_1, is also generated by the ageostrophic current v_1, but it is due to a local, rather than coastal, divergence (convergence) of v_1. The terms labeled with the subscript 2 are due to Ekman pumping in the interior ocean, and they occur wherever there is a local divergence (convergence) of the Ekman drift u_1. They are all proportional to an integral of $\mathcal{T}(t)$, and so continue to increase throughout a wind event. Note that the currents u_2 and v_2 are in geostrophic balance with p_2. Because Y_y is typically much smaller than $\alpha Y(0)$ at the coast [$Y_y = 0$ at the coast for the choice (11)] u_2 does not vanish there, and so this bounded forcing does produce a coastal alongshore current. Finally, p_2 vanishes at the coast, and does not affect coastal sea level.

For a southward wind field with the spatial and temporal structure (10)–(12), u_2 and v_2 describe two counter-rotating gyres, with an anticyclonic gyre on the west flank of the wind axis, and a symmetric cyclonic gyre on its east flank. Associated with these gyres are coastal currents that converge toward the wind axis and an offshore geostrophic flow centered on the axis. As estimated by (A10), the maximum speeds of the coastal and offshore currents (after 6 days) are 344 cm/s and 204 cm/s, respectively, and the maximum Ekman drift (at 3 days) is 68 cm/s. Also as estimated

by (A10); the largest drop in coastal sea level (at 3 days) is 14.1 cm, somewhat smaller than the value for a uniform wind.

Note that there are no coastal Kelvin waves in (17). This is surprising because Kelvin waves are usually generated whenever the interior flow field has a component normal to the coast. For example, when the wind is directed alongshore and is upwelling favorable, part of the interior flow field is offshore Ekman drift, which causes a net transport of water from the coast. In this case, Kelvin waves are a necessary part of the coastal response; they establish a coastal jet that supplies the water for the offshore transport in the forcing region. In solution (17), however, the normal component has two parts, namely, the ageostrophic current $v_1' = (\tau_o/f^2 H)XYT_t$ and the geostrophic current $v_2' = (c^2\tau_o/f^2 H)X_{xx}Y \int_0^t T(r)\, dr$, and neither of them involves a net transport of water normal to the coast (since $\int_0^\infty v_1'\, dt = 0$ and $\int_{-\infty}^\infty v_2'\, dx = 0$). It is because of the particular temporal and zonal structures of these currents that Kelvin waves are not part of the coastal response [see the discussion of Eqs. (A4) and (A6) in the Appendix].

c. Numerical solutions to the linear model

Figure 6 shows the response of the linear model to the Tehuantepec forcing at 3 and 6 days when f is constant. The time development of the solution closely follows that of the analytic solution (17). At day 3, coastal sea level has dropped 17.5 cm in response to offshore ageostrophic flow during the first 3 days [corresponding to v_1 in (17)], and sea level is dropping offshore east of the wind axis and rising west of the axis due to Ekman pumping. The value of 17.5 cm, in fact, underestimates the actual drop because it occurs at a grid point 2.5 km offshore (for the fine grid with a resolution of 5 km); extrapolating to the coast yields a drop of 18.5 cm. At this time the flow field consists of Ekman drift (u_1) and geostrophic currents (u_2 and v_2), but there is no ageostrophic meridional flow (v_1) since $T_t = 0$ at 3 days. The maximum Ekman drift, visible as the zonal component to the flow along the wind axis, is 67 cm/s. At day 6, coastal sea level has returned to normal due to onshore ageostrophic flow (v_1) from day 3 to day 6. The circulation consists of two nearly symmetric gyres in geostrophic balance with the sea-level field. The maximum and minimum values of the coastal currents are $+139$ cm/s and -119 cm/s west and east of the wind axis, and the maximum speed of the offshore flow is 172 cm/s. There is no indication in any of the panels of the propagation of Kelvin waves along the coast.

There are several notable differences between the solution in Figure 6 and the corresponding analytic one. For example, the maximum geostrophic current speeds are all less in the numerical solution; the weakening of the coastal currents is especially pronounced, because the numerical model has no-slip boundary conditions. The westward coastal current is smaller than the eastward one, so that the solution is not completely symmetric about the wind axis near the coast. Perhaps most interesting, the
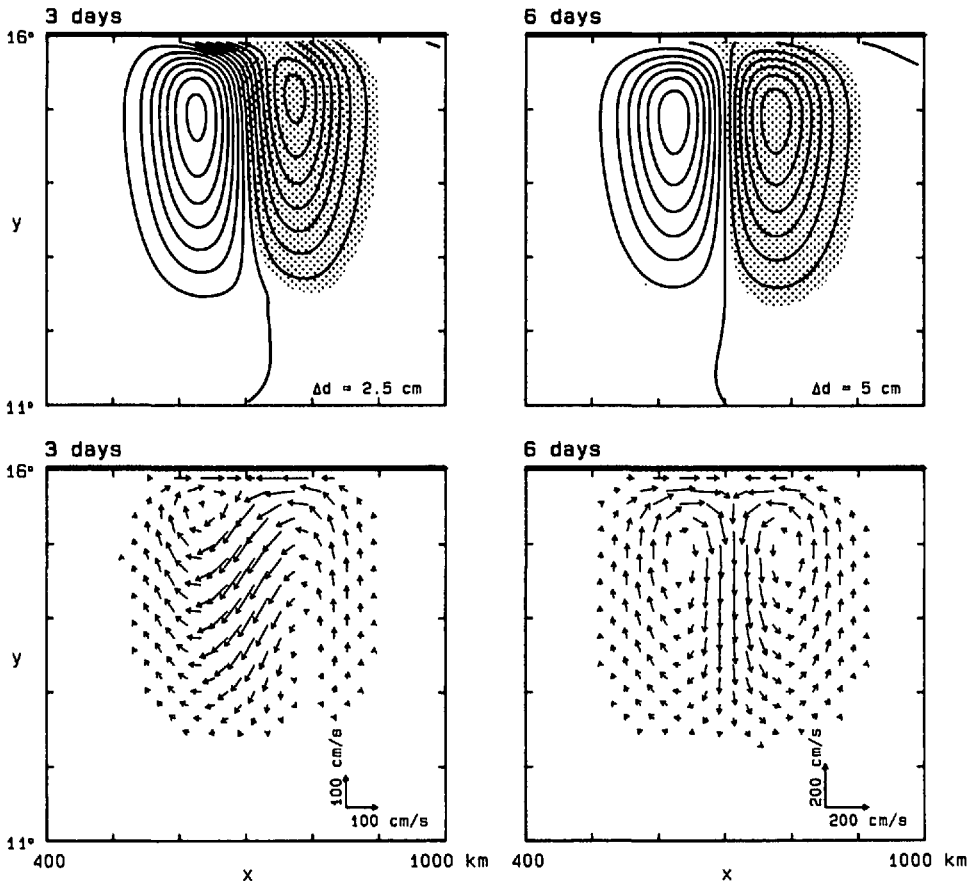
Figure 6. Sea level and currents in the linear model in response to the Tehuantepec forcing for constant f. The contour intervals are 2.5 cm and 5 cm, and the shaded regions indicate where sea level is less than -1.25 cm and -2.5 cm, in the upper left and upper right panels, respectively. After 3 days sea level drops 17.5 cm at the coast. There is Ekman drift across the axis of the jet, and two symmetric, geostrophically balanced gyres are developing offshore due to Ekman pumping. After 6 days the drop in sea level at the coast has vanished, and the two gyres are fully developed. No coastal Kelvin waves propagate westward out of the forcing region.

drop in coastal sea level is significantly *more* than that of the analytic solution. These differences must be due to the presence of horizontal mixing in the numerical model, since otherwise the two systems are dynamically identical. To verify this conclusion, we repeated the numerical calculation without any horizontal mixing. Except for weak inertial oscillations, the resulting solution was essentially the same as solution (A9); in particular, the speeds and locations of the maximum currents and the maximum drop in coastal sea level were nearly identical to those of solution (A10).
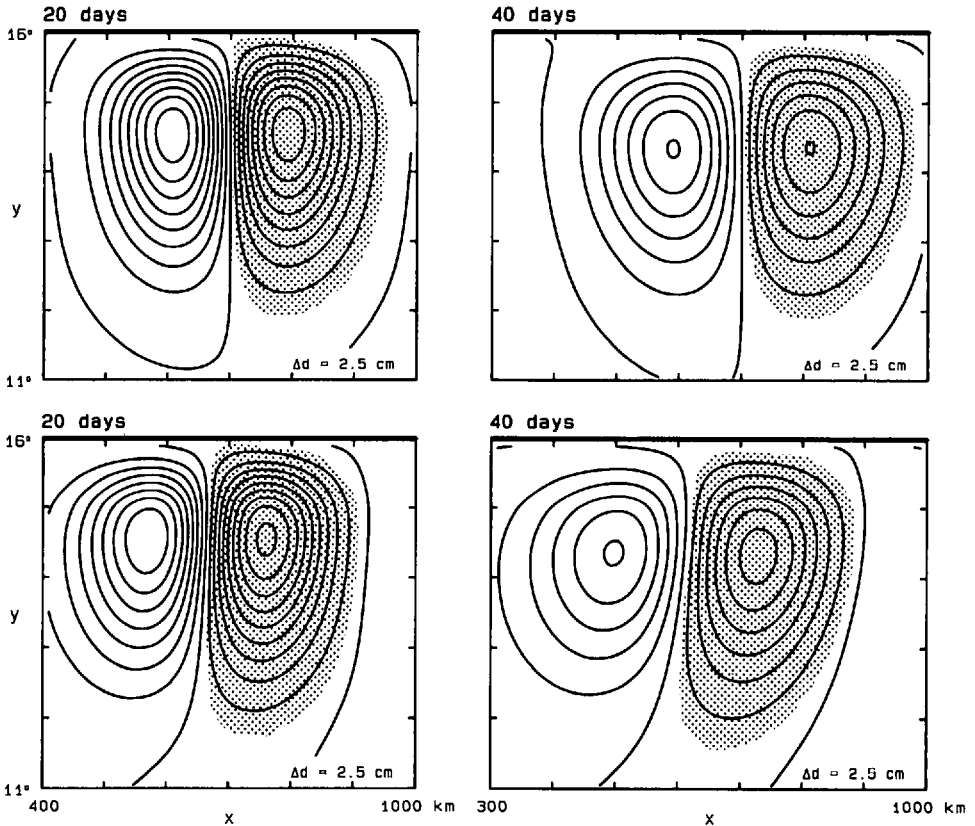
Figure 7. Sea level in the linear model in response to the Tehuantepec forcing, contrasting constant-f (upper panels) and variable-f (lower panels) solutions. The contour interval is 2.5 cm, and the shaded regions indicate where sea level is less than -1.25 cm. When f is constant the two gyres slowly increase in size and weaken due to horizontal mixing. When f is variable the two gyres propagate westward and disperse as a packet of Rossby waves. The dispersion slightly strengthens the cyclonic gyre and weakens the anticyclonic gyre.

Figure 7 contrasts the response for constant f (upper panel) and for variable f (lower panel) at 20 and 40 days. With f constant, the two gyres slowly increase in size and weaken in strength, but remain symmetric. The inviscid solution (17) remains steady after day 6, suggesting that these changes are due to the horizontal mixing in the numerical model. Indeed, in the numerical calculation without horizontal mixing, the flow field also remained steady after day 6. With f variable, the two gyres propagate westward as a packet of Rossby waves and lose their symmetry. Dispersive effects are apparent in that the cyclonic gyre strengthens somewhat relative to the anticyclonic one. The propagation speed of the anticyclonic gyre is about 3.3 km/day, close to the speed of linear, nondispersive Rossby waves at 14.5N, namely $\beta g' H/f^2 = 3.5$ km/day.
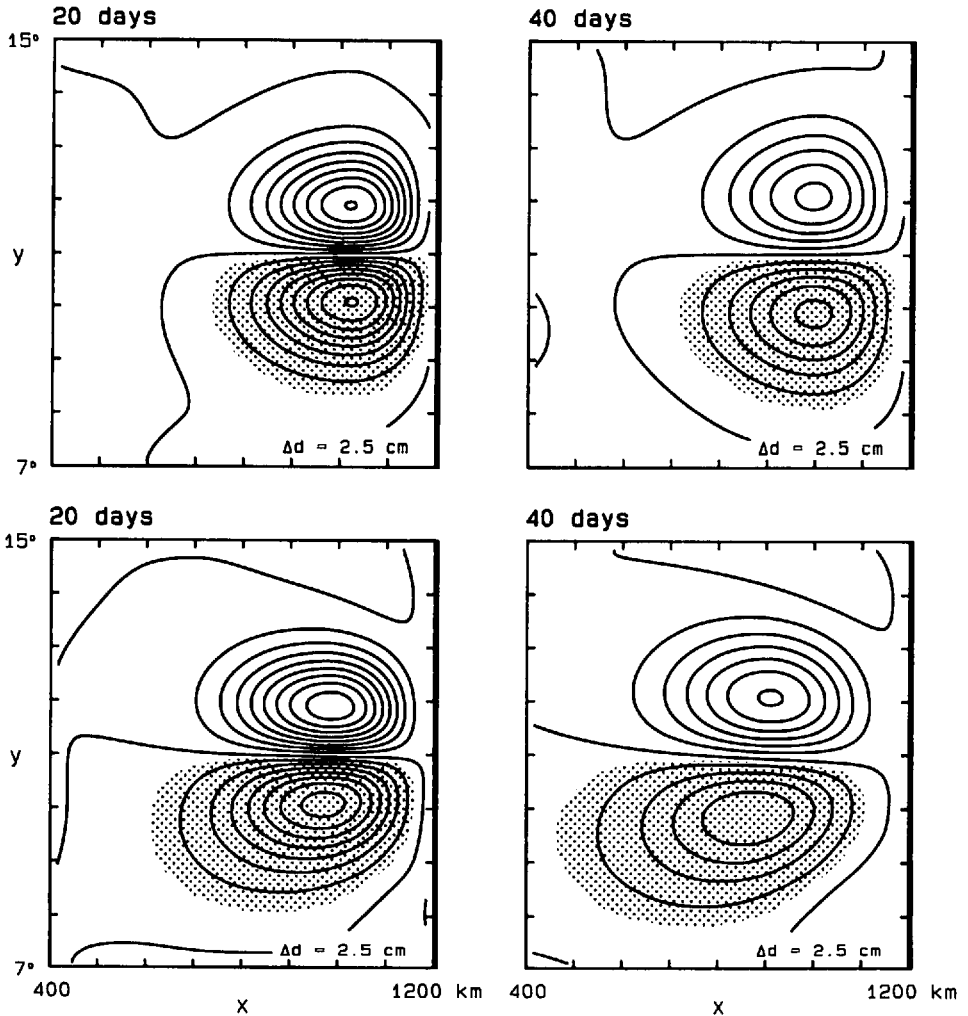
Figure 8. Sea level in the linear model in response to the Papagayo forcing, contrasting constant-f (upper panels) and variable-f (lower panels) solutions. The contour interval is 2.5 cm, and the shaded regions indicate where sea level is less than -1.25 cm. When f is constant (upper panels) the response is similar to that in Figure 7. When f is variable, the cyclonic gyre propagates westward faster than the anticyclonic gyre due to the increase of the propagation speed of Rossby waves toward the equator.

Figure 8 contrasts the constant-f and variable-f responses at 20 and 40 days for the Papagayo forcing. The constant-f solution is similar to that in Figure 6, except that its strength is somewhat larger due to the smaller value of f used ($2.77 \times 10^{-5}\mathrm{s}^{-1}$, instead of $4 \times 10^{-5}\mathrm{s}^{-1}$). With f variable, the cyclonic gyre propagates westward faster than the anticyclonic gyre, consistent with the increase in the propagation speed of Rossby

waves toward the equator. The propagation speed of the anticyclonic gyre, however, is only 3.8 km/day, considerably smaller than the nondispersive Rossby-wave speed at 12N of 5.3 km/day. This difference may be due to the small meridional scale ℓ^{-1} of the wave packet in Figure 8, so that $\beta/(\alpha^2 + \ell^2)$ is a more accurate estimate for the Rossby-wave speed.

d. Numerical solutions to the nonlinear model

Figure 9 illustrates the response of the nonlinear model to Tehuantepec forcing when f is variable, showing sea level, the velocity and temperature fields, and the layer thickness at 3 and 6 days. After 3 days the currents and sea level are similar to their linear counterparts in Figure 6, with sea level dropping 17.4 cm a distance of 2.5 km from the coast (the extrapolated drop at the coast is 18.0 cm). SST is cooled by entrainment in a broad region on and to the east of the wind axis. It reaches an absolute minimum of 19.5°C at the coast (on the fine grid) due to the upwelling induced by offshore ageostrophic flow, and a relative minimum of 21.5°C offshore due to entrainment caused by Ekman pumping. Because of entrainment, the shallowing of the h-field east of the wind axis is much less than its deepening to the west. After 6 days, effects due to advection and entrainment are apparent in all the fields. Most striking is the lack of symmetry of the two gyres. The anticyclonic gyre is stronger and more circular in shape than in the linear solution, and the cyclonic gyre has almost vanished. Tongues of low sea level and of both cold and warm temperature advect around the anticyclonic gyre. Nearly all regions where h is less than H have vanished. At the coast sea level approaches its initial value, and SST rises to 25.0°C. Coldest temperatures now occur well offshore, where SST has dropped to a minimum of 17.7°C. Note that there is an indication in the sea-level and h fields of the westward propagation of a coastal Kelvin wave that acts to *raise,* rather than lower, sea level.

In order to determine how horizontal mixing affects the solution, we repeated the calculation using different values of mixing parameters. With only κ_h reduced to 2×10^6 cm^2/s, gridscale noise appeared by day 5 and increased throughout the integration (40 days). Thus, strong mixing of T is essential for model stability. It is needed to smooth out sharp temperature fronts that continually develop due to advection by the highly sheared flow field. With only ν_h reduced to 2×10^6 cm^2/s, gridscale noise again was visible by day 5, increased until day 10, but diminished thereafter, suggesting that large mixing of momentum is necessary only during the spin-up stage when the currents are strongest. In addition, in this run the maximum drop in coastal sea level at 3 days was only 12.0 cm, demonstrating that larger momentum mixing intensifies the coastal sea-level response in the nonlinear, as well as the linear, model. [It is worth noting that we also explored the effect of horizontal mixing on h, by including the term $\kappa_h \nabla^2 h$ on the right-hand side of the h equation in (4a). The motivation for this investigation was that mixing on h was necessary for model stability in the calculations reported by McCreary and Kundu (1988). The solutions here, however, were not much
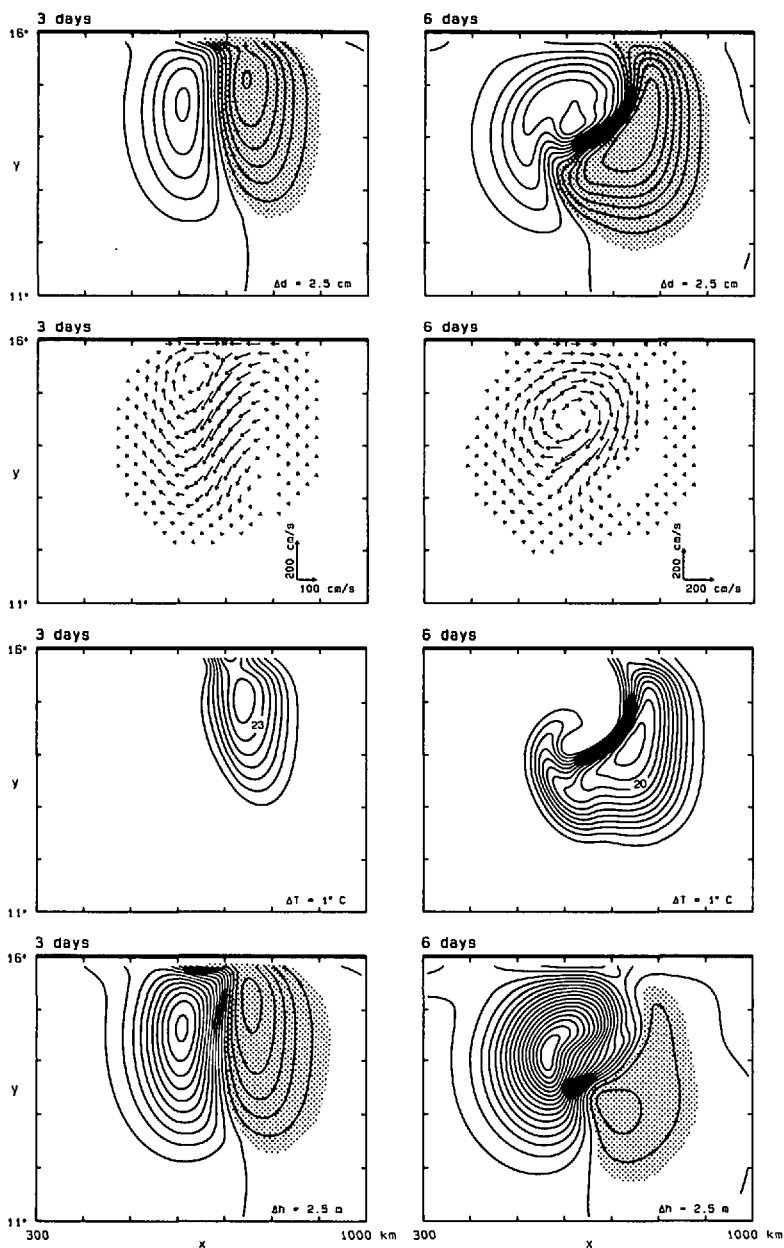
Figure 9. The response of the nonlinear model to the Tehuantepec forcing for variable f, showing sea level, currents, temperature and layer thickness. Contour intervals are 2.5 cm for sea level, 1°C for temperature and 2.5 m for layer thickness. The shaded regions indicate where sea level is less than −1.25 cm and where layer thickness is less than 48.75 m. After 3 days sea level drops 17.4 cm at the coast, the flow field consists of westward Ekman drift plus developing gyres, and SST drops markedly along and east of the wind axis due to entrainment. The lowest temperature (19.5°C) occurs at the coast. After 6 days, the drop in sea level at the coast has almost vanished, the cyclonic gyre has nearly been eliminated by entrainment, and the lowest temperature (17.7°C) now occurs well offshore. The advection terms strengthen the anticyclonic gyre and make it more circular. Tongues of both cold and warm water wrap around the gyre. The sea level and h fields indicate the presence of a coastal Kelvin wave that raises sea level.

affected by this mixing, apparently because sharp fronts of h never developed in any of them.]

In order to isolate the effects of entrainment and advection, we repeated the calculation of Figure 9 without the advection terms in any of Eqs. (4a); in the h equation the expression $(hu)_x + (hv)_y$ was replaced by $h(u_x + v_y)$. The Kelvin wave remained in the solution, indicating that entrainment was its cause; in effect, the Kelvin wave is required in order to create a westward coastal current that removes the excess water introduced into the upper layer by coastal upwelling. The cyclonic gyre was still drastically weakened, clearly the result of the entrainment east of the wind axis. The anticyclonic gyre was very similar in shape to the linear one in Figure 6, and did not attain the more circular form in Figure 9. In addition, there were no tongues of warm and cold SST wrapping around the anticyclonic gyre. The advection terms are obviously the cause of these latter features.

Figure 10 shows the Tehuantepec solution at 20 and 40 days for variable f. The size of the gyre increases rapidly from day 6 to day 20 and continues to increase thereafter. There is a corresponding weakening of the currents during this time, with speeds dropping from about 150 cm/s at day 6 to 30 cm/s at day 40. SST warms considerably due to the surface heat flux Q, which relaxes T back to 29°C in a time scale of 50 days. The circulation pattern propagates westward due to β with a speed of 5.3 km/day, considerably faster than that of the linear solution in Figure 7 (3.3 km/day). To determine the cause of the larger propagation speed, we carried out a series of test calculations in which we linearized various nonlinear terms in the equations of motion. Only when the terms hp_x and hp_y in (4a) were replaced by Hp_x and Hp_y did the gyre travel westward at the slower, linear Rossby-wave speed. An important effect of these nonlinear terms is that nondispersive Rossby waves propagate at the "local" speed $\beta g'h/f^2$, rather than $\beta g'H/f^2$. Thus, the primary reason for the increased propagation speed of the gyre is the larger layer thickness at its center, resulting in an enhanced, local Rossby-wave speed. At day 30, for example, $h = 75.7$ m and $T = 27.7$°C at the center of the gyre, and the local Rossby-wave speed at 14N is 5.3 km/day, the same value as the model result.

In an additional test run investigating the effects of horizontal mixing, we repeated the calculation of Figures 9 and 10 with ν_h (but not κ_h) reduced to 2×10^6 cm^2/s *after* day 6. Because ν_h was decreased after the spin-up stage, very little noise subsequently developed. The solution differed significantly from the response in Figure 10 in that the broadening and weakening of the gyre did not occur, demonstrating that momentum mixing was the cause of these changes. At day 40, for example, the diameter of the gyre was only about 300 km and the maximum current speed was somewhat greater than 80 cm/s. In addition, the westward propagation speed of the gyre increased to 7.3 km/day. One reason for this increase is that h was larger at the center of the stronger gyre (88.5 m at 30 days) resulting in an enhanced, local Rossby-wave speed. Another cause is the advection associated with the much stronger flow field, as discussed next.
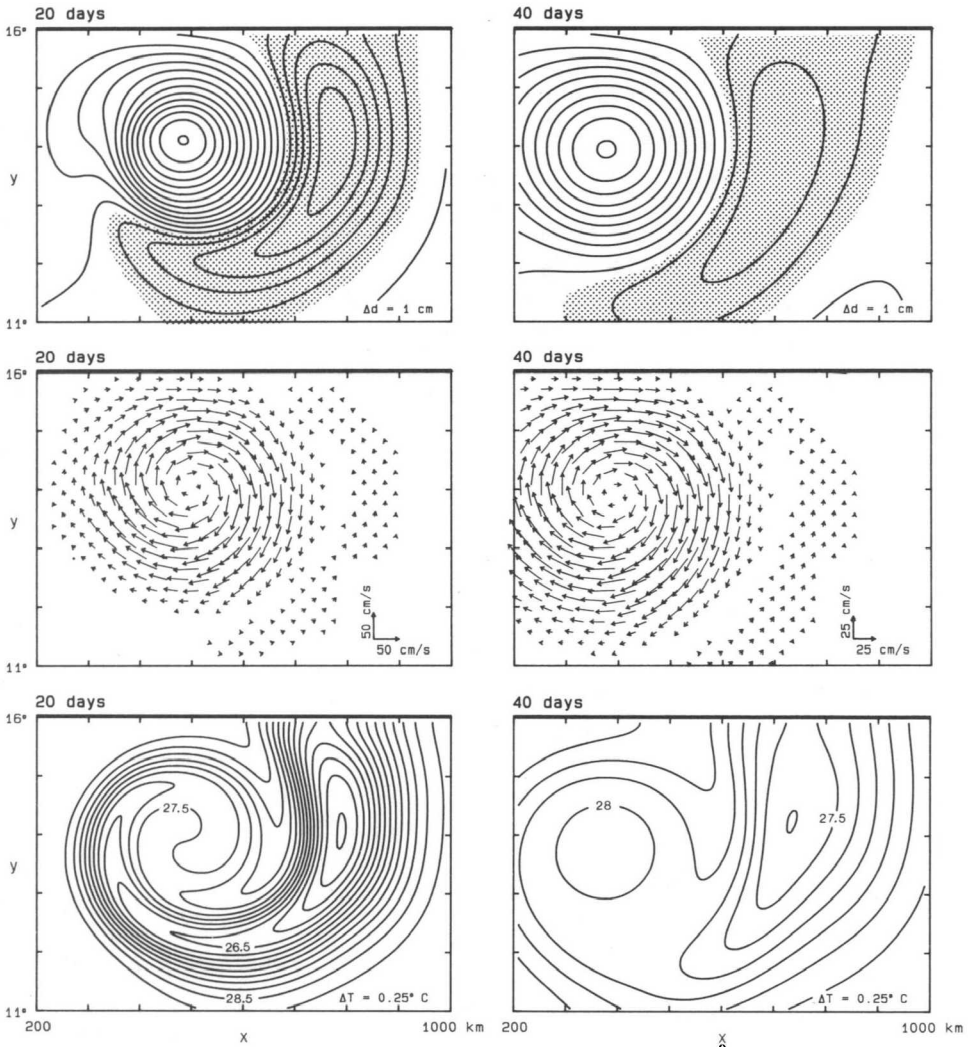
Figure 10. As in Figure 9, except at 20 and 40 days. The shaded regions indicate where sea level is less than −.5 cm. Contour intervals are 1 cm for sea level and .25°C for temperature. The anticyclonic gyre propagates westward and increases in size. Its propagation speed is 5.3 km/day, significantly faster than that of the linear solution in Figure 7. Cool SST is warmed considerably by surface heating after 40 days.

The initial response of the model to Papagayo forcing is very similar to that of the Tehuantepec case. Figure 11 shows the solution for variable f after 20 and 40 days when ν_h is decreased to 2×10^6 cm^2/s at day 6. Because ν_h is reduced, the gyre does not markedly broaden and weaken, and at day 40 its diameter and maximum current speed are roughly 300 km and 110 cm/s, respectively. (If ν_h is not decreased, the gyre diameter and current speeds are 500 km and 25 cm/s at 40 days, similar to the
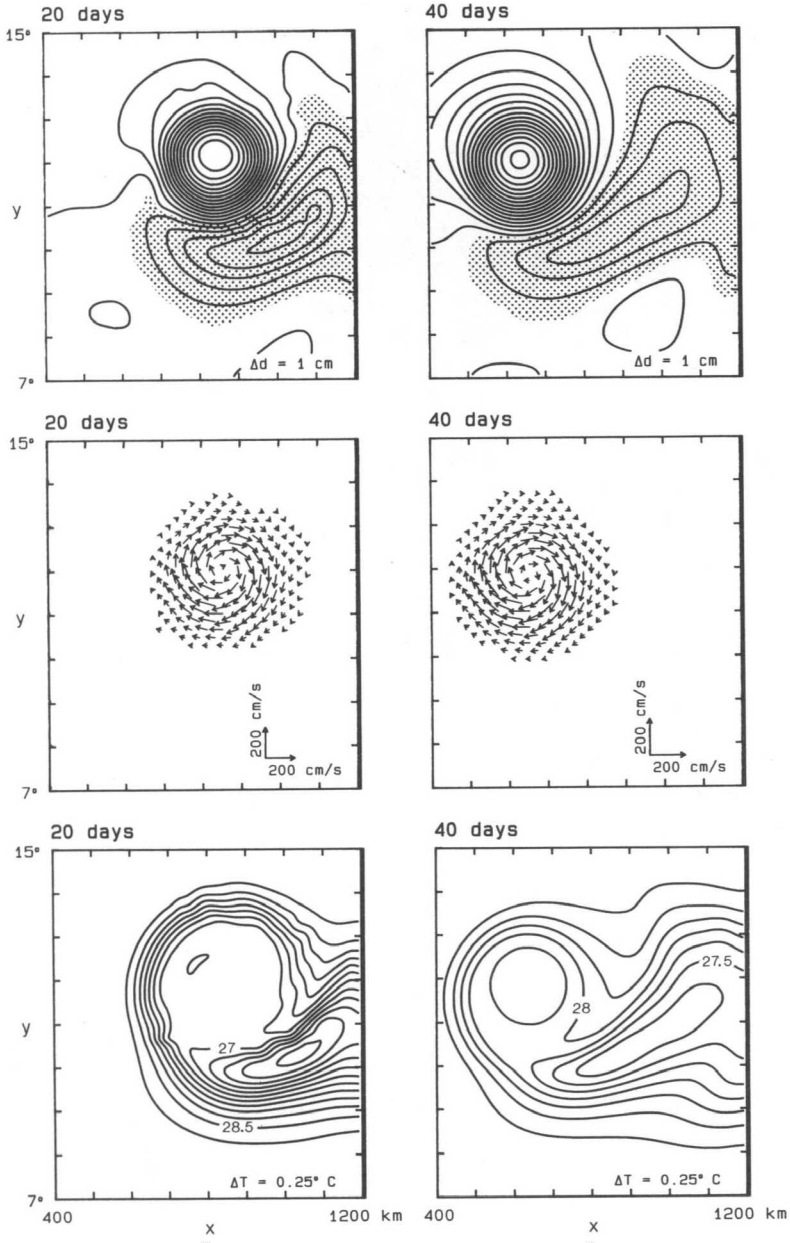
Figure 11. The response of the nonlinear model to the Papagayo forcing for variable f when ν_h is decreased to 2×10^6 cm^2/s at day 6, showing sea level, currents and temperature. Contour intervals are 1 cm for sea level and .25°C for temperature. The shaded regions indicate where sea level is less than $-.5$ cm. In contrast to the Tehuantepec case in Figure 10, the anticyclonic gyre does not broaden and weaken. Its westward propagation speed is 10.3 km/day, much larger than that of the linear solution in Figure 8. Cool SST warms due to surface heating.

Tehuantepec case in Fig. 10). The westward propagation speed of the gyre is 10.3 km/day, much faster than that of the linear solution in Figure 8 (3.8 km/day). This speed is also significantly larger than the local Rossby-wave speed; at day 30, values for h and T at the center of the gyre are 87.5 m and 27.3°C, and the local Rossby-wave speed at 14N is only 8.3 km/day. In one test calculation, we replaced the terms hp_x and hp_y in (4a) with Hp_x and Hp_y, and the propagation speed decreased, but only to 8.4 km/day. In a second, we also neglected the momentum flux divergence in the momentum equations and the propagation speed decreased to 5.0 km/day, a value close to the linear Rossby-wave speed (5.3 km/day). Thus, the increased propagation speed has two nonlinear causes: the terms associated with the larger layer thickness at the center of the gyre, and the momentum flux divergence. The latter mechanism is more influential in this case, because current speeds are much larger for the gyre in Figure 11 than for the one in Figure 10.

Finally, we repeated the Tehuantepec and Papagayo runs using modified forms of entrainment. In one set of calculations w_e was set to zero at day 6, a plausible change since the wind stress also vanishes at this time. Solutions were not significantly different at later times, indicating that the important effects of entrainment happened during the first 6 days of integration. In another set of calculations H_e was reduced at all times to 30 m. The resulting solutions were similar to those in Figures 9, 10 and 11 except for the following differences: the appearance of cool SST was delayed for more than two days until h became less than H_e, and the cyclonic flow was considerably stronger because h could remain less than H. In the Papagayo run, for example, the structure of the cyclonic flow field was similar to that shown in Figure 11 (indicated by the shaded regions in the upper panels), but its maximum speed was half that of the anticyclonic gyre.

4. Summary and discussion

In this paper we investigate the response of the coastal ocean to forcing by wind stress fields similar in structure to the narrow mountain-pass jets that occur in the Gulfs of Tehuantepec and Papagayo during the fall and winter. These jets blow directly offshore at speeds of the order of 25 m/s. They are typically about 200 km wide, extent 500 km offshore, and last for 3 to 10 days. The ocean models used are linear and nonlinear versions of a 1½-layer model. The nonlinear version also includes an equation for the upper-layer temperature field with entrainment, and so generates an SST field. Solutions are arranged in a hierarchy of increasing dynamical complexity, and are obtained both analytically and numerically.

Analytic solutions are found with f constant. The simplest solution is forced by a spatially uniform, meridional wind field in an unbounded basin [solution (14)]. It develops an ageostrophic v field that accounts for the coastal upwelling in all the other solutions. The next solution adds a northern boundary to the ocean [solution (16)]. In this case, there is a sea level response at the coast that is directly proportional to the wind stress, but no coastal currents are generated. Other solutions are forced by

spatially confined wind fields like the mountain-pass jets [solutions (17), (A9) and (A10)]. They develop two symmetric gyres offshore due to Ekman pumping, have strong coastal currents that converge on the wind axis, and do not generate any coastal Kelvin waves.

Numerical solutions to the linear model with f constant corroborate the analytic results (Fig. 6), and demonstrate that horizontal mixing strengthens the coastal sea level response (Fig. 6) and slowly broadens and weakens the symmetric gyres (Figs. 7 and 8). When f is variable, the gyres propagate westward with a speed less than that of nondispersive Rossby waves, and lose their symmetry (Figs. 7 and 8).

Entrainment, nonlinearities and mixing all affect the solutions to the nonlinear model. Entrainment cools SST and almost eliminates the cyclonic gyre by preventing the thickness of the layer h from becoming much less than its initial value H (Fig. 9). The advection terms strengthen the anticyclonic gyre, give it a more circular shape, and create tongues of warm and cold water that wrap around the anticyclonic gyre (Fig. 9). Both the nonlinear terms associated with the increase in layer thickness at the center of the gyre and the momentum flux divergence increase its westward propagation speed over that predicted by linear theory (Figs. 10 and 11). As for the linear model, momentum mixing strengthens the coastal sea-level response (Fig. 9). It also broadens and weakens the anticyclonic gyre, and slows its propagation speed (compare Figs. 10 and 11).

The solutions presented here, particularly those of the nonlinear model, compare remarkably well with the available observations, suggesting that the models contain much of the important dynamics of the phenomenon. On the other hand, the model Papagayo gyres propagate westward somewhat more slowly than the observed ones (at 10.3 km/day, as compared to 13 km/day). In addition, it is worrisome that aspects of solutions (particularly coastal sea level and gyre propagation speed) are sensitive to mixing parameters. Finally, the elimination of the cyclonic gyre by entrainment is a nice feature of the nonlinear model, but the observations are as yet insufficient to verify conclusively that entrainment is the reason for its absence in the real ocean. Further theoretical and, more importantly, observational studies are needed.

APPENDIX

Derivation of analytic solutions

In this appendix we find exact and approximate solutions to the inviscid version of Eqs. (1) with f constant. They are forced by a meridional wind field with separable

spatial and temporal structure, as in (9). The method of solution utilizes Laplace transforms in time and Fourier transforms in x, defined by

$$\hat{q}(s) = \int_0^\infty e^{-st} q(t) \, dt, \qquad \tilde{q}(k) = \int_{-\infty}^\infty e^{-ikx} q(x) \, dx, \qquad (A1)$$

respectively. Transforming and rewriting Eqs. (1) gives

$$\hat{\tilde{p}}_{yy} - \kappa^2 \hat{\tilde{p}} = \frac{ik}{s} f \hat{\tilde{G}} + \hat{\tilde{G}}_y,$$

$$\hat{\tilde{u}} = \frac{-iks\hat{\tilde{p}} - f\hat{\tilde{p}}_y + f\hat{\tilde{G}}}{s^2 + f^2}, \qquad (A2)$$

$$\hat{\tilde{v}} = \frac{ikf\hat{\tilde{p}} - s\hat{\tilde{p}}_y + s\hat{\tilde{G}}}{s^2 + f^2},$$

where $\hat{\tilde{G}} = (\tau_o/H)\tilde{X}(k)Y(y)\hat{T}(s)$ and $\kappa^2 = k^2 + (s^2 + f^2)/c^2$. The solution proceeds by solving the first of Eqs. (A2) for $\hat{\tilde{p}}$, and then $\hat{\tilde{u}}$ and $\hat{\tilde{v}}$ are known in terms of $\hat{\tilde{p}}$. It is convenient in the following to represent solutions to (A2) as the sum of two pieces: a forced response in an unbounded ocean (designated by a prime) and a superposition of free waves excited at the coast (designated by double primes).

The solution to the first of Eqs. (A2) for the forced pressure field is

$$\hat{\tilde{p}}' = \frac{ikf}{2\kappa s}\left(e^{\kappa y}\int_{+\infty}^y e^{-\kappa y'}\hat{\tilde{G}}dy' - e^{-\kappa y}\int_{-\infty}^y e^{\kappa y'}\hat{\tilde{G}}dy'\right)$$
$$+ \frac{1}{2\kappa}\left(e^{\kappa y}\int_{+\infty}^y e^{-\kappa y'}\hat{\tilde{G}}_{y'}\,dy' - e^{-\kappa y}\int_{-\infty}^y e^{\kappa y'}\hat{\tilde{G}}_{y'}\,dy'\right), \qquad (A3)$$

and it follows from the last of Eqs. (A2) that

$$\hat{\tilde{v}}' = -\frac{s^2\kappa^2 + k^2 f^2}{2s\kappa(s^2 + f^2)}\left(e^{\kappa y}\int_{+\infty}^y e^{-\kappa y'}\hat{\tilde{G}}\,dy' - e^{-\kappa y}\int_{-\infty}^y e^{\kappa y'}\hat{\tilde{G}}dy'\right). \qquad (A4)$$

The interior current $\hat{\tilde{v}}'$ has two parts: one proportional to $s\kappa$, $\hat{\tilde{v}}_1'$, and the other to $k^2 f^2/(\kappa s)$, $\hat{\tilde{v}}_2'$. [The large-scale and slowly varying versions of $\hat{\tilde{v}}_1'$ and $\hat{\tilde{v}}_2'$ invert to produce the ageostrophic current v_1' and the geostrophic current v_2' (defined near the end of section 3b), respectively.] As discussed next, the particular structures of $\hat{\tilde{v}}_1'$ and $\hat{\tilde{v}}_2'$ ensure that no Kelvin waves are part of the coastal response.

The coastal response is a solution of the homogeneous version of (A2) that decays as $y \to -\infty$; its pressure field is

$$\hat{\tilde{p}}'' = \hat{\tilde{P}}(k, s)e^{\kappa y}, \qquad (A5)$$

where the amplitude $\hat{\tilde{P}}(k, s)$ is independent of y. The coastal boundary condition,

$\hat{v}'' = -\hat{v}'$ at $y = 0$, then requires that

$$
\begin{aligned}
\hat{\bar{P}}(k, s) &= \frac{s^2 + f^2}{s\kappa - ikf} \hat{\bar{v}}'_0 = \frac{s^2 + f^2}{s\kappa - ikf} [(\hat{v}'_1)_0 + (\hat{v}'_2)_0] \\
&= -\left(\frac{1}{2} + \frac{ikf}{2s\kappa}\right)\left(\int_{+\infty}^{0} e^{-\kappa y'} \hat{\bar{G}} dy' - \int_{\infty}^{0} e^{\kappa y'} \hat{\bar{G}} dy'\right),
\end{aligned}
\tag{A6}
$$

where the subscript zero indicates that the fields are evaluated at $y = 0$. Note that, because $\hat{v}'_0$ contains the factor $s^2\kappa^2 + k^2f^2$, the denominator $s\kappa-ikf$ cancels out. It is this pole that produces Kelvin waves in the system. Its absence means that no Kelvin waves can be generated by a wind blowing perpendicular to a coast, a property noted previously by Crepon and Richez (1982) for a y-independent wind field.

The total pressure field, $\hat{\bar{p}} = \hat{\bar{p}}' + \hat{\bar{p}}''$, can be written

$$
\begin{aligned}
\hat{\bar{p}} &= \frac{ikf}{2\kappa s}\left(e^{\kappa y} \int_{0}^{y} e^{-\kappa y'} \hat{\bar{G}} \, dy' - e^{-\kappa y} \int_{-\infty}^{y} e^{\kappa y'} \hat{\bar{G}} \, dy'\right) \\
&+ \frac{1}{2\kappa}\left(e^{\kappa y} \int_{0}^{y} e^{-\kappa y'} \hat{\bar{G}}_y \, dy' - e^{-\kappa y} \int_{-\infty}^{y} e^{\kappa y'} \hat{\bar{G}}_y \, dy'\right) \\
&+ \left(\frac{ikf}{2\kappa s} + \frac{1}{2}\right) e^{\kappa y} \int_{-\infty}^{0} e^{\kappa y'} \hat{\bar{G}} \, dy' + \frac{1}{2\kappa} e^{\kappa y} \hat{\bar{G}}_0
\end{aligned}
\tag{A7}
$$

after an integration by parts of one of the terms in (A3). There are similar expressions for $\hat{\bar{u}}$ and $\hat{\bar{v}}$. Note that none of the integrals in (A7) extends into the region $y > 0$ (that is, over land), a feature that obviously must hold. It is interesting that $\hat{\bar{p}}$ does not vanish at the coast, another property noted earlier by Crepon and Richez (1982) for a y-independent forcing. As discussed in the text, this response is forced by a meridional, ageostrophic current, rather than by Ekman drift.

Now suppose that the wind is large scale in y, in that $(L_y\alpha)^{-2} \equiv \epsilon^2 \ll 1$ where L_y is the meridional length scale of the wind. Integrations by parts of the y-integrals in (A7) generate series of terms accurate to increasingly higher orders of ϵ, and the series can be truncated at $0(\epsilon)$. The resulting expressions for $\hat{\bar{u}}$, $\hat{\bar{v}}$ and $\hat{\bar{p}}$ are

$$
\begin{aligned}
\hat{\bar{u}} &= \frac{ik}{s\kappa^2} (\hat{\bar{G}}_y - \kappa\hat{\bar{G}}_0 e^{\kappa y}) + \frac{f}{c^2\kappa^2} (\hat{\bar{G}} - \hat{\bar{G}}_0 e^{\kappa y}), \\
\hat{\bar{v}} &= \frac{k^2 + s^2/c^2}{s\kappa^2} (\hat{\bar{G}} - \hat{\bar{G}}_0 e^{\kappa y}), \\
\hat{\bar{p}} &= -\frac{ikf}{s\kappa^2} (\hat{\bar{G}} - \hat{\bar{G}}_0 e^{\kappa y}) - \frac{1}{\kappa^2} (\hat{\bar{G}}_y - \kappa\hat{\bar{G}}_0 e^{\kappa y}).
\end{aligned}
\tag{A8}
$$

For the meridional profile (11) and model parameters used in this paper $(L_y\alpha)^{-2} = [(\pi/2y_w)(c/f)]^2 = .024$, and solution (A8) is very accurate.

Suppose further that the wind is also slowly-varying in time, in that $(L_t f)^{-2} \equiv \epsilon^2 \ll 1$ where L_t is the time scale of the wind. This approximation means that $\hat{T}(s)$ is appreciable only in the region $|s|^2 \ll f^2$. As a result, most of the contributions to the Laplace inversion integrals occur in this region, and it is possible to obtain a solution accurate to $0(\epsilon^2)$ by neglecting s^2 in κ everywhere in (A8). With the aid of the Fourier convolution theorem, the resulting solution is

$$u = \frac{\tau_o}{fH} [(E * X)Y - (K_i * X)Y(0)]T$$

$$+ \frac{\tau_o}{\alpha^2 H} [(E * X_x)Y_y - (K * X_x)\alpha Y(0)] \int_0^t T(r)\, dr,$$

$$v = \frac{\tau_o}{f^2 H} [(E * X)Y - (K_i * X)Y(0)]T_t$$

$$\hspace{6cm} \text{(A9)}$$

$$- \frac{\tau_o}{\alpha^2 H} [(E * X_{xx})Y - (K_i * X_{xx})Y(0)] \int_0^t T(r)\, dr,$$

$$p = \frac{\tau_o}{\alpha^2 H} [\alpha(K * X)Y(0) - (E * X)Y_y]T$$

$$- \frac{f\tau_o}{\alpha^2 H} [(E * X_x)Y - (K_i * X_x)Y(0)] \int_0^t T(r)\, dr.$$

The function $E(x) = (\alpha/2) \exp(-\alpha|x|)$, $K(x, y) = (\alpha/\pi)K_0 [\alpha(x^2 + y^2)^{1/2}]$ where K_0 is a modified Bessel's function, $K_i = \int_{-\infty}^{y} \alpha K\, dy'$, and the convolution operator is defined by $q * \chi = \int_{-\infty}^{\infty} q(x - x', y)\chi(x')\, dx'$. For the time dependence (12), $(L_t f)^{-2} = [(2\pi/t_w)(1/f)]^2 = .09$ and solution (A9) is reasonably accurate. It differs from the exact solution primarily in that it lacks the weak inertial oscillations excited by a slowly varying wind. The solutions of Crepon and Richez (1982) are essentially given by (A9) with $X(x)$ being either a step or a ramp function, $T(t)$ being a step function, and $Y(y) = 1$.

Now, the functions E, K and K_i are all sharply peaked weighting functions $q(x, y)$ that decay rapidly outside a Rossby radius of either $x = 0$ (for E) or the origin (for K and K_i). For the choice of $X(x)$ in (10), it is possible to take advantage of this property to obtain a solution that is accurate at points interior to the wind patch, that is, at positions x located more than a Rossby radius from the eastern and western edges of the patch. For such points, the contributions to the convolution integrals, $q * \chi$, from regions near the edges are negligible because $q(x - x', y)$ is small there. In other words, the response does not "feel" the edges of the wind. Thus, we can safely ignore the edges of the wind in (10), replacing $X(x)$ with the upper expression in (10) for all x. In that case, all the convolution integrals in (A9) can be evaluated analytically, and the

resulting solution is

$$u = \frac{\tau_o}{fH}\left[\frac{1}{2}\left(1 + \frac{\alpha^2}{\gamma^2}\cos\xi\right)Y - \frac{1}{2}\left(e^{\alpha y} + \frac{\alpha^2}{\gamma^2}\cos\xi\, e^{\gamma y}\right)Y(0)\right]T(t)$$

$$+ \frac{\tau_o}{\gamma^2 H}X_x[Y_y - \gamma Y(0)e^{\gamma y}]\int_0^t T(r)\,dr,$$

$$v = \frac{\tau_o}{f^2 H}\left[\frac{1}{2}\left(1 + \frac{\alpha^2}{\gamma^2}\cos\xi\right)Y - \frac{1}{2}\left(e^{\alpha y} + \frac{\alpha^2}{\gamma^2}\cos\xi\, e^{\gamma y}\right)Y(0)\right]T,$$

$$\qquad\qquad\qquad\qquad\qquad\qquad\qquad\qquad\qquad\qquad\qquad\qquad\qquad\text{(A10)}$$

$$- \frac{\tau_o}{\gamma^2 H}X_{xx}[Y - Y(0)e^{\gamma y}]\int_0^t T(r)\,dr,$$

$$p = \frac{\tau_o}{\alpha^2 H}\left[\frac{1}{2}\left(\alpha e^{\alpha y} + \frac{\alpha^2}{\gamma}\cos\xi\, e^{\gamma y}\right)Y(0) - \frac{1}{2}\left(1 + \frac{\alpha^2}{\gamma^2}\cos\xi\right)Y_y\right]T(t)$$

$$- f\frac{\tau_o}{\gamma^2 H}X_x[Y - Y(0)e^{\gamma y}]\int_0^t T(r)\,dr,$$

where $\gamma = [(2\pi/x_w)^2 + \alpha^2]^{1/2}$ and $\xi = 2\pi(x - x_m)/x_w$. [It is easier in this case to obtain (A10) directly from (A8), without using the convolution theorem as in (A9).]

Solution (A10) provides accurate estimates for the maximum values attained by the fields, since all the maxima occur well inside the edges of the wind patch. For the wind field and parameter values used in this paper, the maximum speed of the coastal currents, occuring after 6 days at the positions $x = x_m \pm x_w/4$, is $(|\tau_o|/\gamma H)$ $(\pi/x_w)(t_w/2) = 344$ cm/s. The maximum offshore flow happens at 6 days on the wind axis at $y = y_1 = y_m - 94$ km, where y_1 is the position that maximizes the function $\mathcal{Y}_1$ $(y) = Y(y) - Y(0)e^{\gamma y}$; its value is $2(|\tau_o|/\gamma^2 H)(\pi/x_w)^2\mathcal{Y}_1(y_1)(t_w/2) = 203$ cm/s. The strongest ageostrophic meridional flow occurs at days 1.5 and 4.5 on the wind axis at $y = y_2 = y_m - 99$ km, where y_2 is the position that maximizes the function $\mathcal{Y}_2(y) =$ $(1 + \alpha^2/\gamma^2)Y - Y(0)(e^{\alpha y} + \alpha^2 e^{\gamma y}/\gamma^2)$, its value is $(|\tau_o|/f^2 H)\mathcal{Y}_2(y_2)(\pi/2t_w) =$ 10 cm/s. Similarly, the maximum Ekman drift occurs at day 3 on the wind axis at $y = y_2$, and has the value $(|\tau_o|/fH)\mathcal{Y}_2(y_2)/2 = 68$ cm/s. The largest drop in coastal sea level occurs at day 3 on the wind axis and is $(|\tau_o|/g\alpha H)(1 + \alpha/\gamma)/2 = 14.1$ cm.

Finally, suppose that the wind is also large scale in x, in that $(L_x\alpha)^{-2} \equiv \epsilon^2 \ll 1$ where L_x is the zonal scale of the wind. Then it is possible to obtain a solution that is accurate to $0(\epsilon^2)$ by replacing κ with α throughout (A8). With this replacement the transforms in (A8) are easily inverted to obtain solution (17). For the choice of $X(x)$ in (10), $(L_x\alpha)^{-2} = [(2\pi/x_w)(c/f)]^2 = .79$, which is not much less than 1. Thus, although the basic structure and time development in (17) is correct, it has aspects that are not accurate. For example, expressions for the maximum values of the coastal currents, offshore current and sea level are just those in the preceding paragraph with γ replaced by α; the resulting maxima are 460 cm/s, 345 cm/s at $y_1 = -109$ km and 16.1 cm, respectively, all larger than the more accurate estimates provided by (A10).

REFERENCES

Crepon, M. and C. Richez. 1982. Transient upwelling generated by two-dimensional atmospheric forcing and variability in the coastline. J. Phys. Oceanogr., *12*, 1437-1457.

Enfield, D. B. and J. S. Allen. 1983. On the structure and dynamics of monthly mean sea level anomalies along the Pacific coast of North and South America. J. Phys. Oceanogr., *10*, 557–578.

Haney, R. L. 1971. Surface thermal boundary conditions for ocean circulation models. J. Phys. Oceanogr., *1*, 241–248.

Hansen, D. V. 1987. History and status of the NOAA EPOC5 program, *in* Further Progress in Equatorial Oceanography, E. J. Katz and J. M. Witte, eds., Nova University Press.

Hua, B. L. and F. Thomasset. 1983. A numerical study of the effects of coastline geometry on wind-induced upwelling in the Gulf of Lions. J. Phys. Oceanogr., *13*, 678–694.

McCreary, J. P. and P. K. Kundu. 1988. A numerical investigation of the Somali Current during the southwest monsoon. J. Mar. Res., *46*, 25–58.

Roden, G. I. 1961. On the wind-driven circulation in the Gulf of Tehuantepec and its effect upon surface temperatures. Geofis. Int., *1*, 55-72.

Stumpf, H. G. 1975. Satellite detection of upwelling in the Gulf of Tehuantepec, Mexico. J. Phys. Oceanogr., *5*, 383–388.

Stumpf, H. G. and R. V. Legeckis. 1977. Satellite observations of mesoscale eddy dynamics in the eastern tropical Pacific Ocean. J. Phys. Oceanogr., *7*, 648–658.